Fan Delta Uplift and Mountain Subsidence during the 2010 Haiti Earthquake

Manabu Hashimoto[1)*], Yo Fukushima[1)], and Yukitoshi Fukahata[1)]

1) Disaster Prevention Research Institute, Kyoto University
Gokasho, Uji, Kyoto 611-0011, Japan

*) Corresponding author

The relative motion between the Caribbean and North American plates is accommodated by several active faults and folds in and around Hispaniola Island (1–3). The Enriquillo-Plantain Garden fault (EPGF) in southern Haiti is one of these structures (2, 4), and a strain equivalent to an Mw 7.2 event is estimated to have accumulated along this fault since its last major activity (4). The Haiti earthquake of 12 January 2010 was initially reported to have occurred along this fault (5, 6), but more recent studies proposed slips on previously unrecognised faults (5, 7-8). Here we show crustal displacement caused by the Haiti earthquake, as detected by interferometric synthetic aperture radar (InSAR). The radar images show uplift of an alluvial fan delta on the north side of the EPGF and subsidence of mountains to its south. By inverting the interferograms using a nonlinear inverse method based on Bayesian modelling (9), the fault was modelled dipping northward at 42°, with large thrust components. Maximum displacement was about 4 m at about 10–20 km depth below the offshore area near the Tiburon peninsula, Haiti. The earthquake indeed ruptured a blind thrust fault that could not be identified from large-scale present-day topography.

The Caribbean and North American plates are converging in an ENE–WSW direction across the east-trending Puerto Rico trench at about 20 mm/yr (Fig. 1). The crustal strain caused by this oblique motion is accommodated by several active faults and folds in and around Hispaniola (1). The NW-trending anticlines on land and offshore (1) imply a NE-oriented compressional stress regime. An uplift rate of 0.37 mm/yr has been estimated for the northwest coast of Hispaniola, whereas a negligible uplift rate has been documented in Gonave Island (1). Global Positioning System (GPS)-based studies have shown that more than two-thirds of the relative plate motion is accommodated by EPGF (~7 mm/yr) and the Septentrional fault (~9 mm/yr), which are considered to be the boundaries between the Gonave microplate and the Caribbean and North American plates, respectively (2, 3). Prior to the 2010 earthquake, the accumulated strain energy in this fault was estimated to be equivalent to an Mw 7.2 event (4).

On 12 January 2010, an Mw 7.0 earthquake occurred in southern Haiti, causing severe damage in and around the capital city of Port-au-Prince (5). More than 220,000 fatalities were reported. Although no surface ruptures were documented (5), the earthquake was initially reported to have ruptured the EPGF (5, 6). The topography west of the epicentre exhibits a clear contrast across the EPGF, with the Quaternary Leogane fan delta on the north side of the fault and a mountain range (Massif de la Selle) on the south side (Fig. 1). The trace of the EPGF is clear between the Leogane fan delta and Port-au-Prince, which suggests major recent high activity.

A seismological study showed that the Haiti mainshock was produced by left-lateral strike-slip with slight reverse motion on a steep (~70°) NNW-dipping plane, but that aftershocks were

44 associated with reverse faulting (~30°–45°) with NNE-oriented P-axes (10). The strike of the
45 nodal plane of the centroid-moment-tensor (CMT) solution (250°) is oblique to the approximately
46 east–west orientation of the EPGF. These observations raise serious questions about the
47 mechanism of the Haiti earthquake, the tectonics of this region, and hazard evaluation. To resolve
48 these conflicts, the coseismic deformation and fault parameters of the Haiti earthquake must be
49 examined.

50 Synthetic aperture radar (SAR) images were used to study coseismic deformation. These images
51 were obtained by the phased-array-type L-band SAR (PALSAR) on Japan's Advanced Land
52 Observation Satellite (ALOS). This system uses longer microwave wavelengths than other SAR
53 sensors, allowing it to penetrate heavily vegetated areas such as tropical forests.

54 Interferograms were computed using four pairs of fine-beam SAR images (three from ascending
55 and one from descending orbits; Supplementary Figs. S1 and S2). Examination of each
56 interferogram revealed artefacts linked to orbital inaccuracies and atmospheric stratification. In
57 areas beyond the deformed region, two types of artefacts were approximated using a bilinear ramp
58 and linearly correlated change with altitude, respectively, and then subtracted from the data. In the
59 corrected ascending interferograms (Fig. 2a), at least six cycles of fringes are evident in the
60 Leogane fan delta. The decrease in range (distance between the satellite and earth's surface) is
61 approximately 70 cm at the centre of these fringes. These fringes are oblique to and cross the
62 EPGF. Other broad fringes that correspond to range increase are evident in the south. In the
63 corrected descending interferogram (Fig. 2b), a cluster of fringes that corresponds to up to 60 cm of

range decrease is also evident in the Leogane fan delta. Another concentric fringe associated with a range decrease is just north of the epicentre. Broad fringes with associated range increase are also present south of the EPGF.

Ascending and descending line-of-sight displacements were converted into quasi-vertical (Fig. 2c) and east–west (Supplementary Fig. S3) components. Azimuth offsets (Supplementary Fig. S4) confirmed that there was a minimal north–south component of the displacement, which implies that the quasi-vertical component (Fig. 3) consisted of predominantly vertical motion. The quasi-vertical displacements indicate uplift of the Leogane fan delta by up to 60 cm, which is consistent with observed uplift of micro-atolls (7). This area also moved westward by up to 80 cm (Supplementary Fig. S3). In contrast, subsidence of up to 40 cm was apparent in the Massif de la Selle, where little east–west motion took place.

ScanSAR images, covering widths of approximately 350 km, provided a deformation map for most of Hispaniola. The original image was divided into five swaths (11) and interferometric analyses were performed for each swath independently (Supplementary Fig. S5). The coherence was very high owing to the small perpendicular baselines (Supplementary Table S1), and the phase continuity between the swaths was good. Coseismic fringes similar to those in Figure 2b are evident, as would be expected from the similarity of the line-of-sight directions. Little deformation was present in the vicinity of the Septentrional fault in northern Haiti.

The slip distribution and dip angle of the fault plane were estimated by inverting the interferograms using a nonlinear inverse method (9) based on Akaike's Bayesian information

84 criterion (ABIC) (12, 13). We assumed a planar fault dipping northward with a strike of 260°,
85 which is roughly consistent with that of the local trace of the EPGF. The location of the upper
86 margin of the fault was determined based on the local topography and the interferograms (Fig. 2c).
87 The modelled fault plane was 102 km long and 0–39 km deep. Both dip and strike components of
88 slip were estimated. As basis functions, we used bicubic B-splines, with 3-km grid spacing in both
89 the strike and depth directions. We searched for the optimal dip angle between 30° and 80°.
90 For inversion inputs, the interferograms were sampled with the quadtree technique (14), with
91 the threshold set to 1.4 rad (~2.6 cm). For ScanSAR interferograms, only the three strips near the
92 epicentre were used. In total, 964 samples were used. Observations along each path were
93 conducted independently, creating offsets between interferograms along different paths. Therefore
94 we also estimated these offsets in the inversion.
95 The optimal model selected according to the ABIC minimum has a dip angle of 42°
96 (Supplementary Fig. S6). The optimal dip angle is much shallower than the 70° of the CMT
97 estimate (10, 15) and instead coincides with those of the aftershocks (10). A difference of two in
98 the ABIC is considered statistically significant. The error in the estimation of the dip angle is
99 about ±3°. Models with a higher dip angle (~70°) produced significantly larger ABICs, which led
100 to rejection of the steeply dipping fault plane geometry (Supplementary Fig. S6). The total
101 variance was reduced by 75%.
102 The distribution of estimated slip and its error (standard deviation) projected onto a vertical
103 plane along the strike of the modelled fault (Fig. 3a, b) shows two patches of large slip at a depth of

104 around 10 km: one is near the hypocenter with a maximum slip of about 3.5 m, and the other is
105 about 20 km to the west with a maximum slip of about 4 m. The estimated geodetic moment was
106 $6.0 \pm 0.9 \times 10^{19}$ N·m (Mw 7.1) using a rigidity of 33 GPa. Thrust motion prevailed in the eastern
107 patch, whereas left-lateral motion was dominant in the western patch. Although slip with an
108 opposing sense is evident on the deep eastern part of the fault plane, the peak amplitude of this slip
109 is as large as the estimated error. These opposing slips suggest that the rupture and the fault's
110 geometry were more complex than had been assumed. A surface projection of the slip distribution
111 with the synthesized interferograms (Fig. 3c, d) indicates that the areas of large slip are located
112 beneath the Leogane fan delta and offshore. This model provides an explanation of the large uplift
113 in the Leogane fan delta obtained by InSAR (Fig. 3c, d; Supplementary Fig. S7).
114 Our estimate of released moment is slightly larger than seismological estimates ($4.4 \sim 4.7 \times 10^{19}$
115 N·m) (6, 10, 15). The discrepancy is attributable to large aftershocks, post-seismic deformation,
116 and uncertainty in the present model and seismological estimates. Large aftershocks spanned by
117 the coseismic interferograms contributed up to 3.9×10^{18} N·m (10). A few previous studies
118 examined the rupture process of this event using a variety of data (InSAR, GPS, micro-atoll, and
119 teleseismic waves) (7, 8). They also reported that dominant moment release occurred in two areas
120 on a north-dipping plane beneath the Leogane fan delta.
121 The most confounding aspect of the 2010 earthquake in Haiti is that the crustal movement
122 shows no correspondence with the present-day large-scale topography: uplift in the Leogane fan
123 delta and subsidence in the mountain range to its south. Although coseismic displacement may be

antithetical to the topographic expression for any given event, the possibility exists that crustal movement may eventually become consistent with topography after the completion of a full earthquake cycle, which includes not only coseismic slip, but also afterslips and viscoelastic relaxation of the asthenosphere. Such a case has been reported for a large interplate earthquake along the Nankai trough, Japan (16). However, considering the location and geometry of the inverted fault and the characteristics of viscoelastic relaxation (17), such a scenario is implausible for this earthquake. Two other possibilities remain. One possibility is that other types of faulting are responsible for the topography. In the 1989 Loma Prieta earthquake in California, Loma Prieta peak, the highest point in the Santa Cruz Mountains, subsided (18, 19). A different fault which uplifts Loma Prieta Peak is suggested to be dominant over a long time scale (20). The other possibility is that the mode of deformation is changing in this region. This may be the case for the 2010 Haiti event because a geological study of the fold-and-thrust belt in central Haiti suggests that a NW-SE trending collision front propagates southward (Figure 1) (21).

The fact that the 2010 Haiti event occurred on a blind thrust fault raises serious concerns regarding the next event. The present model suggests that thrusting occurred on a separate plane from the main strand of the EPGF zone. Although the regional crustal stress is generally thought to have been at least partly released by the 2010 Haiti event, crustal stress, and the consequent seismic risks, may have increased locally (22). Since thrust and fold structures exist in southern Haiti, it is possible that other faults may be reactivated by the increased stress. Detailed modelling

using available geodetic and seismological data will be essential for a more realistic hazard evaluation.

The 2010 Haiti earthquake caused severe damage in the source region, including the capital city, Port-au-Prince. The cause of the damage in Port-au-Prince is controversial. One possibility is the directivity effect of the rupture: seismic energy is amplified in the direction of rupture propagation (23). However, the interferograms and fault model in this study show that the rupture was mainly west of the reported epicentre, which suggests that the rupture propagated from east to west, and that directivity was not responsible for the severe damage in Port-au-Prince. Therefore, the most plausible causes of the damage are poor construction and amplification of seismic waves due to soil conditions.

Method

Geodetic inversion for intraplate earthquakes is usually problematic because of unknown fault locations. However, the nonlinearity is weak if the fault surface can be assumed to be a flat plane. In particular, if any inference occurs in the vicinity of the fault trace, only the dip angle is unknown. Then, the originally nonlinear equation can be rewritten as (9)

$$\mathbf{d} = \mathbf{H}(\delta)\mathbf{a} + \mathbf{e}, \quad (1)$$

where **a** is the model parameter vector for slip, **d** is the observed line-of-sight vector, **e** is the error vector, and **H** is a coefficient matrix that is a function of unknown dip angle δ. Green's function for an elastic half-space with a Poisson's ratio of 0.25 is used.

163 An interferogram usually contains spatially correlated errors that largely come from

164 atmospheric water vapour variation. The error **e** is assumed to be Gaussian with zero mean and

165 covariance $\sigma^2\mathbf{E}$, for which the *ij* component is given as (9)

166 $$E_{ij} = \exp\left(-\frac{r_{ij}}{q}\right), \quad (2)$$

167 where r_{ij} is the distance between the data points *i* and *j*. The correlation distance *q* was assumed to

168 be 10 km (24).

169 In addition, because geodetic inversion is usually poorly constrained, smoothness of slip is

170 commonly assumed as a prior constraint (12). Then, the evaluation function is

171 $$s(\mathbf{a}) = \left[\mathbf{d} - \mathbf{H}(\delta)\mathbf{a}\right]^T \mathbf{E}^{-1}\left[\mathbf{d} - \mathbf{H}(\delta)\mathbf{a}\right] + \alpha^2 \mathbf{a}^T \mathbf{G}(\delta)\mathbf{a} \quad (3)$$

172 in which **G** is a matrix for smoothing, and α^2 defines the relative weight between the data fitting

173 and smoothing condition. The optimal values of α^2, σ^2, and δ, which are called

174 hyperparameters, can be determined with ABIC (9, 12, 13). Once these values have been

175 determined, a solution for **a** can be obtained with the covariance **C**(**a**) by minimizing $s(\mathbf{a})$:

176 $$\mathbf{a} = (\mathbf{H}(\delta)^T \mathbf{E}^{-1}\mathbf{H}(\delta) + \alpha^2\mathbf{G}(\delta))^{-1}\mathbf{H}(\delta)^T\mathbf{E}^{-1}\mathbf{d} \quad (4)$$

177 $$\mathbf{C}(\mathbf{a}) = \sigma^2\left[\mathbf{H}(\delta)^T \mathbf{E}^{-1}\mathbf{H}(\delta) + \alpha^2\mathbf{G}(\delta)\right]^{-1}. \quad (5)$$

178

References

1) Mann, P., Taylor, F.W., Edwards, R.L., & Ku, T-.L. Actively evolving microplate formation by oblique collision and sideways motion along strike-slip faults: an example from the northeastern Caribbean plate margin. *Tectonophysics*, **246**, 1-69 (1995).

2) Mann, P. *et al.* Oblique collision in the northeastern Caribbean from GPS measurements and geological observations, *Tectonics*, **21**, 1057 (2002).

3) DeMets, C., and Wiggins-Grandison, M. Deformation of Jamaica and motion of the Gonave microplate from GPS and seismic data. *Geophys. J. Int.*, **168**, 362-378, (2007).

4) Manaker, D.M. *et al*. Interseismic plate coupling and strain partitioning in the northeastern Caribbean. *Geophys. J. Int.*, **174**, 889-903, (2008).

5) Bilham, R. Lessons from the Haiti earthquake, *Nature*, **463**, 878-879 (2010).

6) U.S. Geological Survey. http://earthquake.usgs.gov/earthquakes/eqinthenews/2010/us2010rja6/ (2010)

7) Hayes, G.P *et al.* Complex rupture during the 12 January 2010 Haiti earthquake, *Nature Geoscience*, **3**, 800-805 (2010).

8) Calais, E. *et al.* Transpressional rupture of an unmapped fault during the 2010 Haiti earthquake, *Nature Geoscience*, **3**, 794-799 (2010).

9) Fukahata, Y., & Wright, T.J. A non-linear geodetic data inversion using ABIC for slip distribution on a fault with an unknown dip angle. *Geophys. J. Int.*, **173**, 353-364, (2008).

10) Nettles, M., & Hjörleifsdóttir, V. Earthquake source parameters for the 2010 Haiti main shock

and aftershock sequence, *Geophys. J. Int.*, **183**, 375-380 (2010).

11) Tong, X., Sandwell, D.T., & Fialko, Y. Coseismic slip model of the 2008 Wenchuan earthquake derived from joint inversion of interferometric synthetic aperture radar, GPS, and field data. *J. Geophys. Res.*, **115**, B04314 (2010).

12) Yabuki, T., & Matsu'ura, M. Geodetic data inversion using a Bayesian information criterion for spatial distribution of fault slip. *Geophys. J. Int.*, **109**, 363-375 (1992).

13) Akaike, H. Likelihood and the Bayes procedure. In: J.M. Bernardo, M.H. DeGroot, D.V. Lindley, and A.F.M. Smith (Editors), *Bayesian Statistics*. University Press, Valencia, 143-166 (1980).

14) Samet, H., & Webber, R.E., Hierarchical data structures and algorithms for computer graphics, *IEEE Computer Graphics & Applications*, **8**, 48-68 (1988).

15) Harvard University. Global CMT Project, http://earthquake.usgs.gov/earthquakes/eqinthenews/2010/us2010rja6/neic_rja6_gcmt.php (2010).

16) Fukahata, Y., Honsho, C., & Matsu'ura, M. Crustal movements on Shikoku, southwestern Japan, inferred from inversion analysis of levelling data using ABIC. *Tectonophysics*, **257**, 239-252 (1996).

17) Fukahata, Y., & Matsu'ura, M. Quasi-static internal deformation due to a dislocation source in a multilayered elastic/viscoelastic half-space and an equivalence theorem. *Geophys. J. Int.*, **166**, 418-434 (2006).

18) Lisowski, M., Prescott, W.H., Savage, J.C., & Johnston, M.J. Geodetic estimate of coseismic slip during the 1989 Loma Prieta, California, earthquake. *Geophys. Res. Lett.*, **17**, 1437-1440 (1990).

19) Marshall, G.A., Stein, R.S., & Thatcher, W. Faulting geometry and slop from co-seismic elevation changes: the 18 October 1998, Loma Prieta, California, earthquake. *Bull. Seismol. Soc. Amer.*, **81**, 1660-1693 (1991).

20) Schwarz, S.Y., Orange, D.L., & Anderson, R.S. Complex fault interactions in a restraining bend on the San Andreas Fault, southern Santa Cruz Mountains, California. *Geophys. Res. Lett.*, **17**, 1207-1210 (1990).

21) Pubellier, M. *et al*. Plate boundary readjustment in oblique convergence: example of the Neogene of Hispaniola, Greater Antilles, *Tectonics*, **19**, 630-648 (2000).

22) Jin, L., Stein, R.S., Sevilgen, V. & Toda, S. USGS-WHOI-DPRI Coulomb stress-transfer model for the January 12, 2010, Mw=7.0 Haiti earthquake, *U.S. Geological Survey Open-File Report* 2010-1019, 7p.

23) Miyake, H., Iwata, T., & Irikura, K., Estimation of rupture propagation direction and strong motion generation area from azimuth and distance dependence of source amplitude spectra. *Geophys. Res. Lett.*, **28**, 2727-2730 (2001).

24) Lohman, R.B. & Simons, M. Some thoughts on the use of InSAR data to constrain models of surface deformation: noise structure and data downsampling, *Geochem. Geophys. Geosyst.*, **6**, Q01007 (2005).

25) Wessel, P., & Smith, W.H.F. New, improved version of Generic Mapping Tools released. *EOS Trans. Amer. Geophys. U.* **79**, 579 (1998).

26) Coffin, M.F., Gahagan, L.M., & Lawver, L.A. Present-day Plate Boundary Digital Data Compilation. *University of Texas Institute for Geophysics Technical Report*, **174**, 5 (1998).

27) DeMets, C *et al.* GPS geodetic constraints on Caribbean–North American plate motion, *Geophys. Res. Lett.*, **27**, 437-440 (2000)

Correspondence and requests for materials should be addressed to M.H.

Acknowledgments

We thank Professor David Sandwell, Scripps Institute of Oceanography, University of California, San Diego, and Rob Mellors, San Diego State University, who kindly permitted us to use their program to process ScanSAR images. We also thank Shinji Toda who made valuable suggestions. The PALSAR level 1.0 data were provided by the Japan Aerospace Exploration Agency (JAXA) via the Geographical Survey Institute as part of the project “Evaluation of Use of ALOS for Disaster Mitigation” of the Earthquake Working Group. The PALSAR product is owned by JAXA and the Ministry of Economy, Trade and Industry, Japan. We used Generic Mapping Tools (25) to prepare illustrations.

Author Contributions

Manabu Hashimoto was the principal researcher of this study and was in charge of analyzing the SAR images and creating the fault slip model. Yo Fukushima was responsible for preparing and developing the InSAR analysis procedures and for removing artefacts in the interferograms. Yukitoshi Fukahata developed the original inversion software for the InSAR data used in this study. All three authors discussed the interferometry results and the tectonic significance of the fault slip model.

Competing Financial Interests

There are no competing financial interests involved in this article.

Figure Captions

Figure 1. Tectonics around Hispaniola. Solid lines are tectonic boundaries and active faults, respectively, obtained from the websites of the University of Texas (26) and the GEO's Haiti Supersite (http://supersites.earthobservations.org/Haitifaults.mat), provided by V. Sevilgen and R. Stein. Dashed lines and hatches show the fold-and-thrust belt (21). The thick pink arrow shows the motion of the Caribbean Plate and Gonave microplate relative to the North American Plate (3, 27). Thin pink arrows indicate the relative slip across the Septentrional fault (SF) and Enriquillo-Plantain Garden fault (EPGF). Red circles are epicentres of aftershocks (6). The inset shows a close-up of the topography around the U.S. Geological Survey-National Earthquake Information Center (USGS-NEIC) epicentre of the mainshock (red star).

Figure 2. Interferograms of strip-map mode images. (a) Ascending and (b) descending interferograms. The star and beach ball indicate the USGS-NEIC epicentre (6) and the centroid-moment-tensor (CMT) solution (15), respectively. Thick yellow and black arrows denote the directions of the line of sight (LOS) and heading of the satellite, respectively. Thin yellow arrows indicate incidence angle. One cycle of colour corresponds to a LOS change of 11.8 cm. The blue–yellow–red–blue change indicates the decrease in range between the Earth's surface and the satellite. White dashed lines indicate active faults. (c) Quasi-vertical component of deformation. The circle denotes the origin for the coordinates used in the inversion process. The solid line is the surface trace of the modelled fault running through the origin with a strike of N 260° E.

Figure 3. Fault model. (a) Slip distribution projected onto a vertical cross section oriented at N 260° E. Estimated dip angle of the fault plane is 42° to the north. Blue arrows are estimated slip vectors. Contours indicate the amount of slip at 20-cm intervals. The star is the projection of the hypocenter of the mainshock (6). (b) Estimated error of slip. Contour interval is 25 cm. Synthetic interferograms: (c) ascending and (d) descending. Rectangle and contours show the surface projections of the fault plane and the slip distribution, respectively. Thick lines with tick marks indicate the upper margin of the fault.

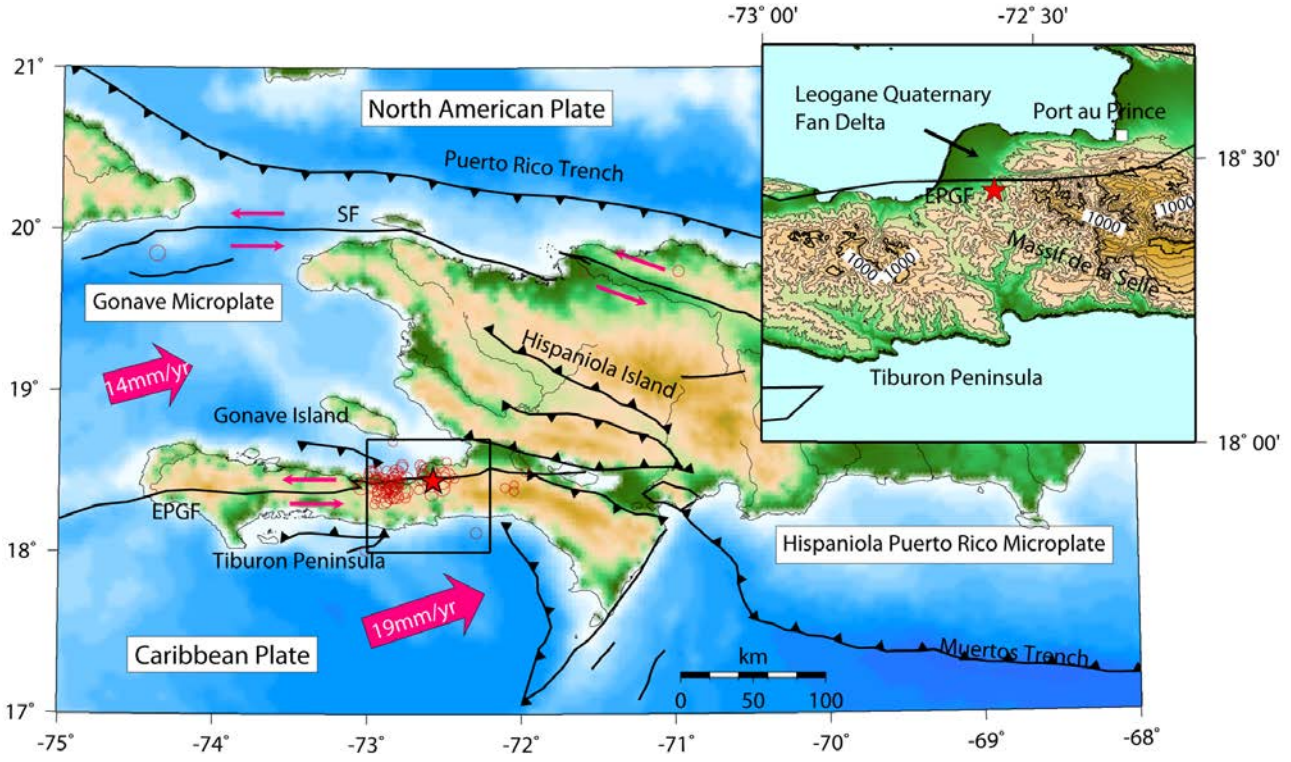

Figure 1. Tectonics around Hispaniola. Solid lines are tectonic boundaries and active faults, respectively, obtained from the websites of the University of Texas (26) and the GEO's Haiti Supersite (http://supersites.earthobservations.org/Haitifaults.mat), provided by V. Sevilgen and R. Stein. The thick pink arrow shows the motion of the Caribbean Plate and Gonave microplate relative to the North American Plate (3, 27). Thin pink arrows indicate the relative slip across the Septentrional fault (SF) and Enriquillo-Plantain Garden fault (EPGF). Red circles are epicentres of aftershocks (6). The inset shows a close-up of the topography around the U.S. Geological Survey-National Earthquake Information Center (USGS-NEIC) epicentre of the mainshock (red star).

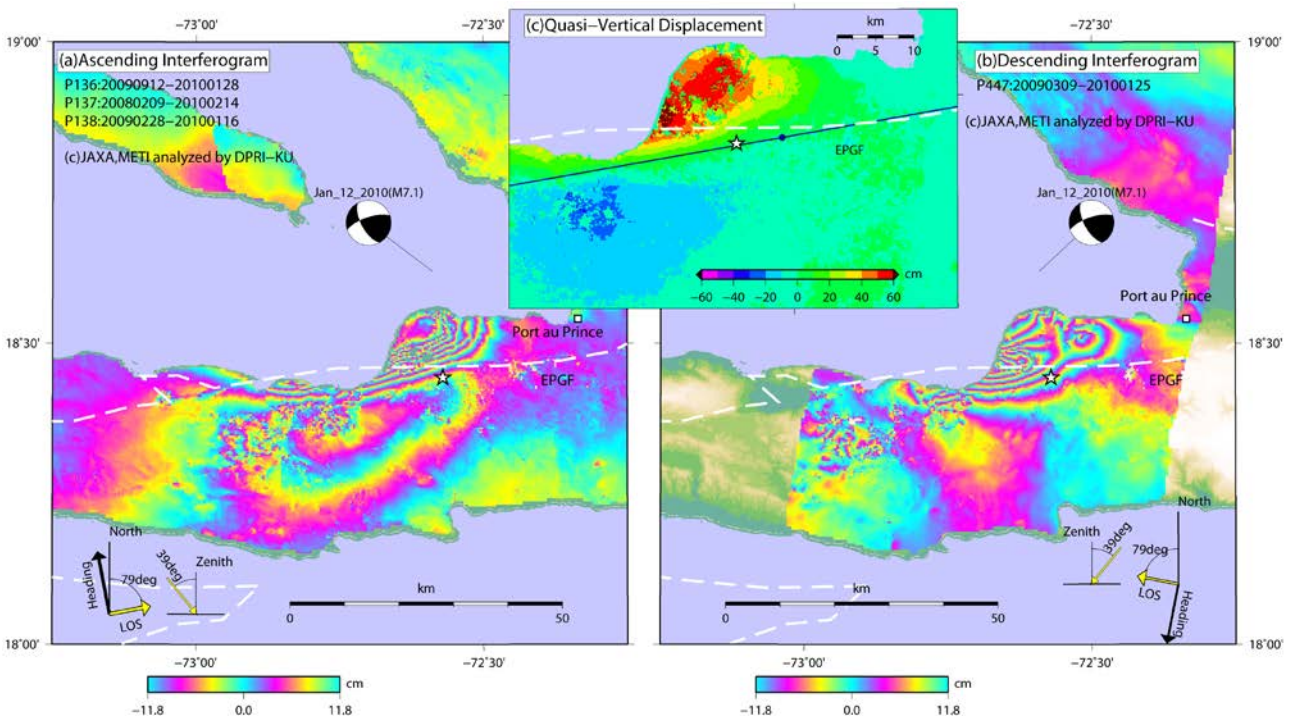

Figure 2. Interferograms of strip-map mode images. (a) Ascending and (b) descending interferograms. The beach ball indicate the USGS-NEIC epicentre (6) and the centroid-moment-tensor (CMT) solution (14), respectively. Thick yellow and black arrows denote the directions of the line of sight (LOS) and heading of the satellite, respectively. Thin yellow arrows indicate incidence angle. One cycle of colour corresponds to a LOS change of 11.8 cm. The blue–yellow–red–blue change indicates the decrease in range between the Earth's surface and the satellite. White dashed lines indicate active faults. (c) Quasi-vertical component of deformation. The circle denotes the origin for the coordinates used in the inversion process. The solid line is the surface trace of the modelled fault running through the origin with a strike of N 260° E.

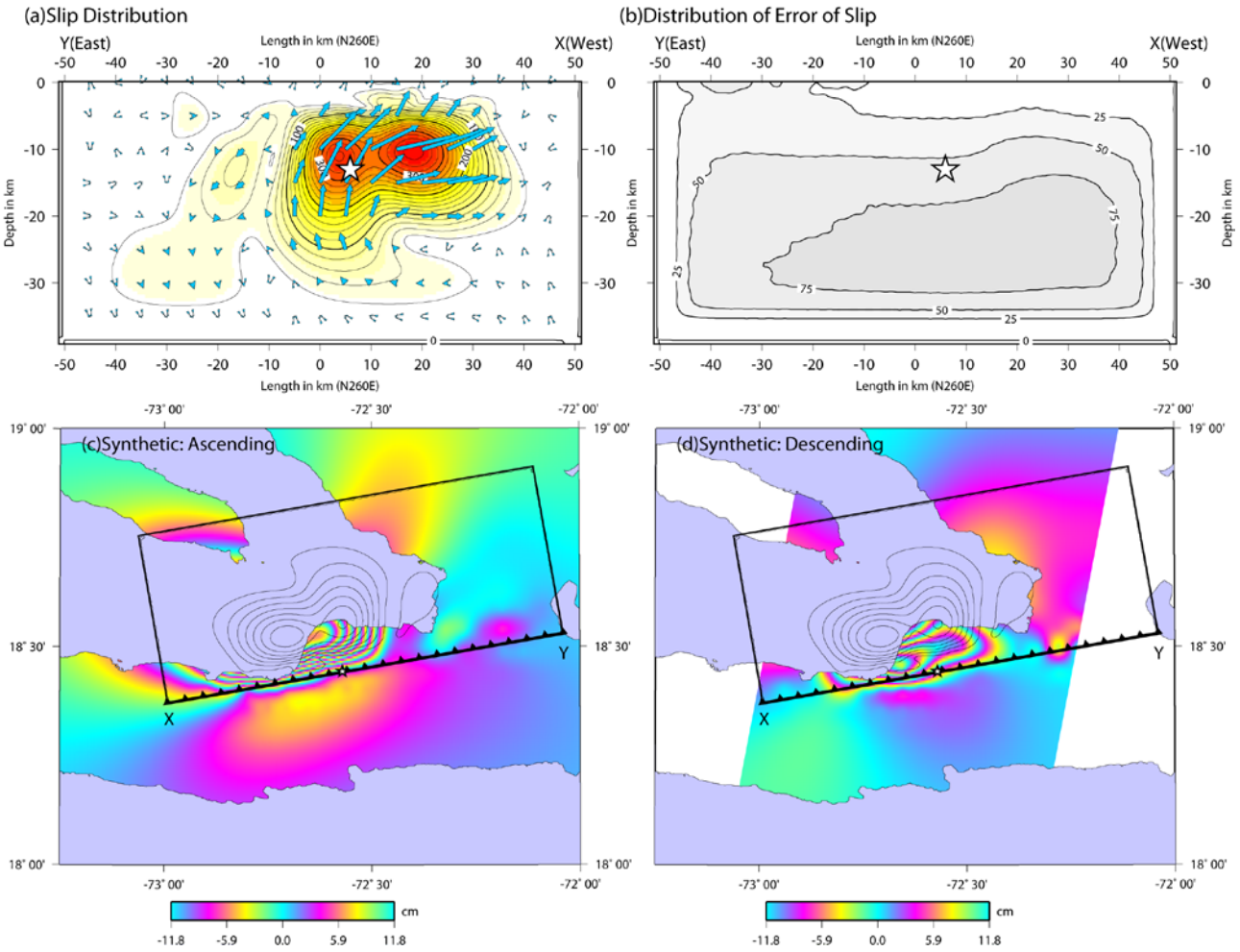

Figure 3. Fault model. (a) Slip distribution projected onto a vertical cross section oriented at N 260° E. Estimated dip angle of the fault plane is 42° to the north. Blue arrows are estimated slip vectors. Contours indicate the amount of slip at 20-cm intervals. The star is the projection of the hypocenter of the mainshock (6). (b) Estimated error of slip. Contour interval is 25 cm. Synthetic interferograms: (c) ascending and (d) descending. Rectangle and contours show the surface projections of the fault plane and the slip distribution, respectively. Thick lines with tick marks indicate the upper margin of the fault.

Supplementary Information

Acquisition and Analyses of ALOS/PALSAR Images

This project is affiliated with the Earthquake Working Group for the Evaluation of ALOS for Use in Disaster Mitigation, led by the Japan Aerospace Exploration Agency (JAXA). JAXA made urgent observations with PALSAR immediately after the Haiti earthquake at the request of the working group. PALSAR can use either of two observation modes for interferometric SAR (InSAR): the high-resolution strip-map mode, which has a swath of about 70 km, and the wide-swath ScanSAR mode, which has a swath of about 350 km. Both types of observation were made for this event.

Before the mainshock, strip-map-mode observations near the epicentre had been made for four different paths: three from ascending orbits and one from a descending orbit. Observations from these four paths were also made after the mainshock for InSAR applications (Supplementary Table S1 and Supplementary Fig. S1). In addition, ScanSAR observations of western Hispaniola had been made from a descending orbit before the mainshock. At the request of the Earthquake Working Group, JAXA acquired images after the mainshock in such a way that the burst timing was synchronized with one of the previous acquisitions, which enabled interferometric analysis.

Two-pass differential interferometry was performed using GAMMA® software with the Consultative Group on International Agricultural Research (CGIAR) hole-filled Shuttle Radar Topography Mission (SRTM) digital elevation model (DEM) (1).

Supplementary Table S1. Properties of the ALOS/PALSAR images used in this study.

Path	Orbit	Mode	Master	Slave	Bperp* (m)	Incidence Angle* (deg)	Number of Sampled Data	Offset (cm)
136	Ascending	Strip	Sep 12 '09	Jan 28 '10	809	38.8	137	-0.6
137	Ascending	Strip	Feb 9 '08	Feb 14 '10	-433	38.8	195	1.1
138	Ascending	Strip	Feb 28 '09	Jan 16 '10	1051	38.8	137	2.5
447	Descending	Strip	Mar 9 '09	Jan 25 '10	812	38.8	215	-1.6
448 (swath1)#	Descending	ScanSAR	Sep 26 '09	Feb 11 '10	260	22.9	-	
(swath2)					237	29.4	42	-0.6
(swath3)					217	34.5	176	-2.5
(swath4)					201	38.5	62	-3.1
(swath5)					193	41.3	-	

* The perpendicular baseline (Bperp) and incidence angle are measured at the scene centre.

In the ScanSAR mode of ALOS, microwaves are repeatedly emitted at five different changing incidence angles. The strip for each incidence angle refers to a swath. The epicentre is located in swath 3.

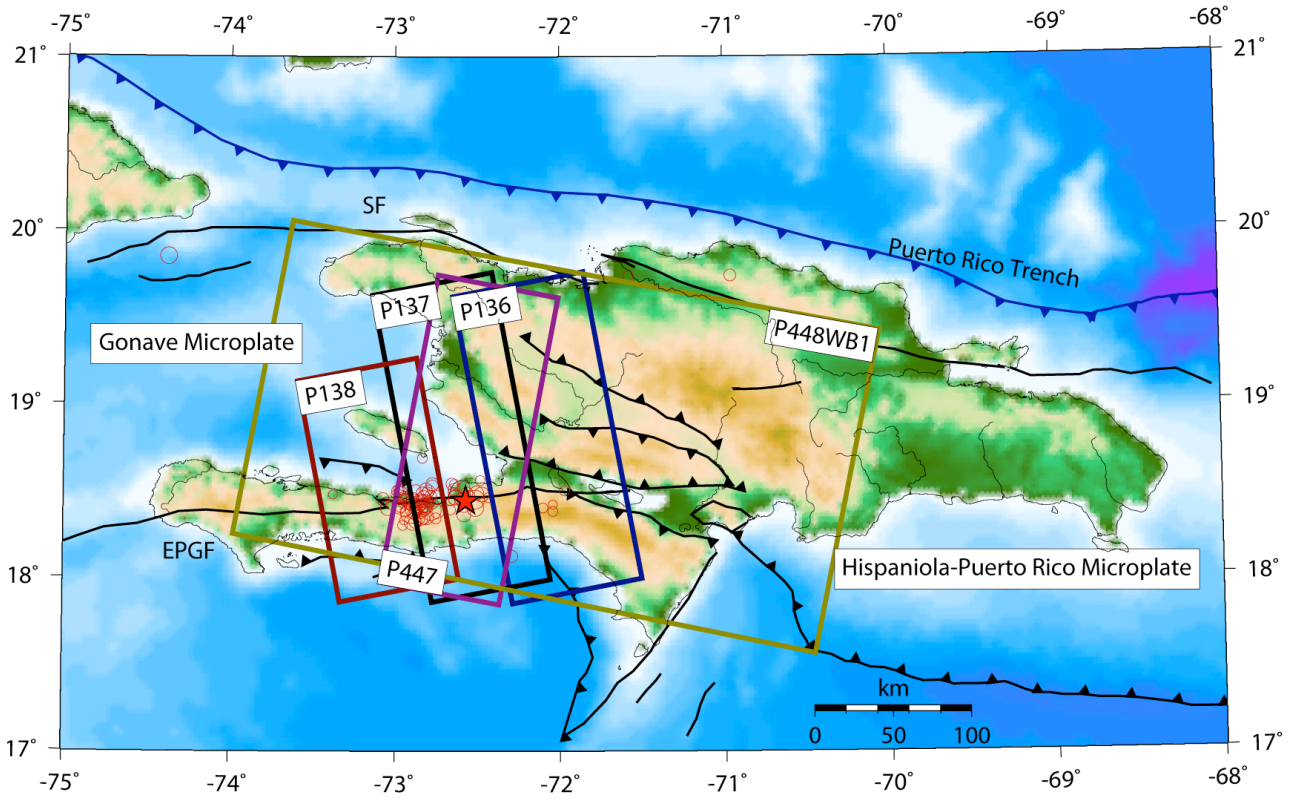

Supplementary Figure S1. Location of the Haiti earthquake and coverage area of ALOS acquisitions. SF and EPGF stand for the Septentrional and Enriquillo-Plantain Garden faults, respectively.

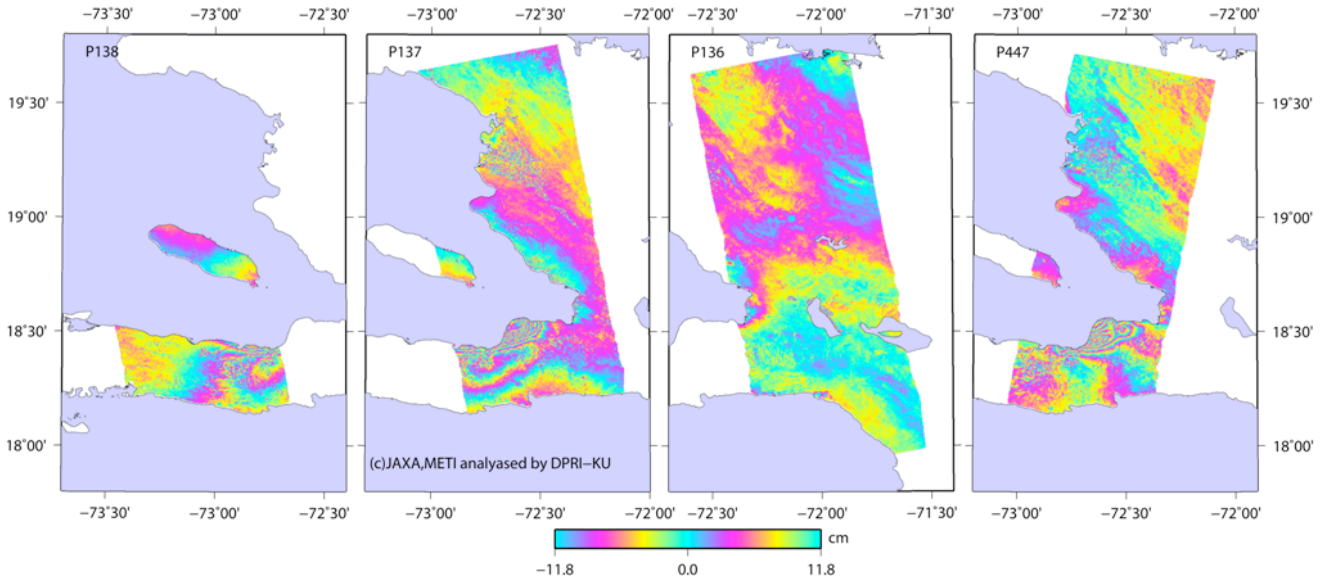

Supplementary Figure S2. Interferograms for the pairs of images acquired using the strip-map mode. Perturbations that could be attributed to tropospheric disturbance or phase ramp are not corrected. Concentric fringes are conspicuous in the Tiburon peninsula.

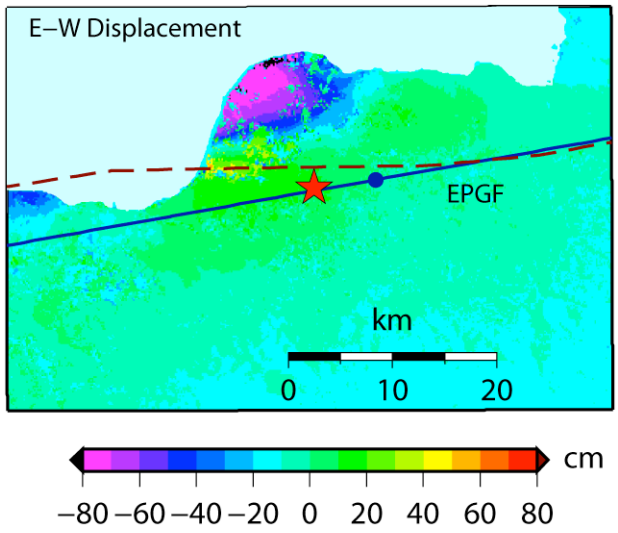

Supplementary Figure S3. East–west components of deformation produced from the unwrapped interferograms from both ascending and descending orbits. Positive values are assigned to eastward components. The star indicates the epicentre of the mainshock. The circle indicates the origin of coordinates used in the inversion process. The solid line is the surface trace of the modelled fault running through the origin with a strike of N 260° E.

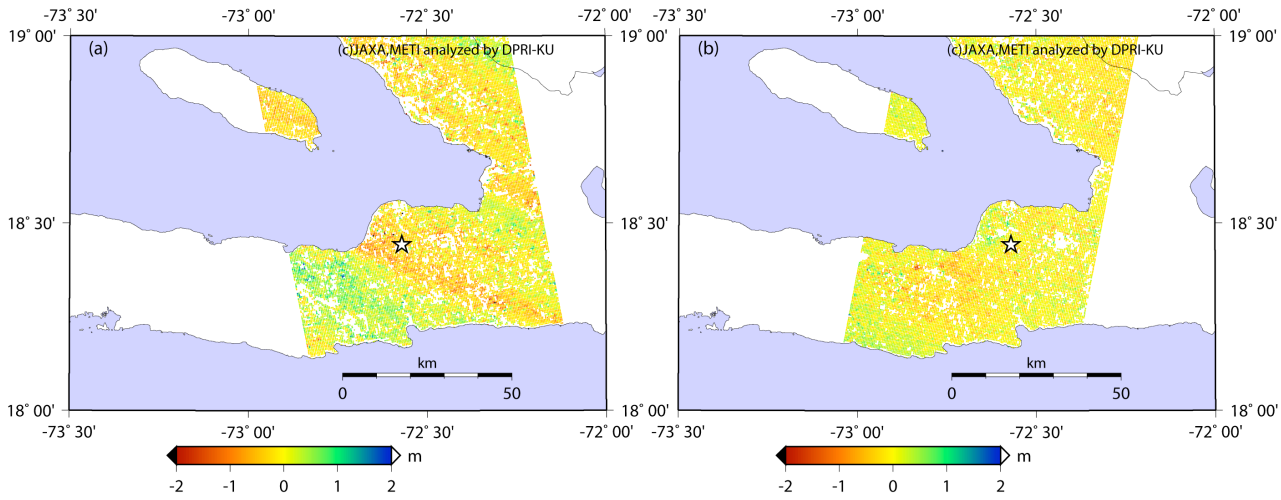

Supplementary Figure S4. **Azimuth offsets**: (a) ascending orbit; (b) descending orbit.

Azimuth offset is displacement in the azimuth direction, which is independent of the range change component and can be estimated with the pixel-matching technique.

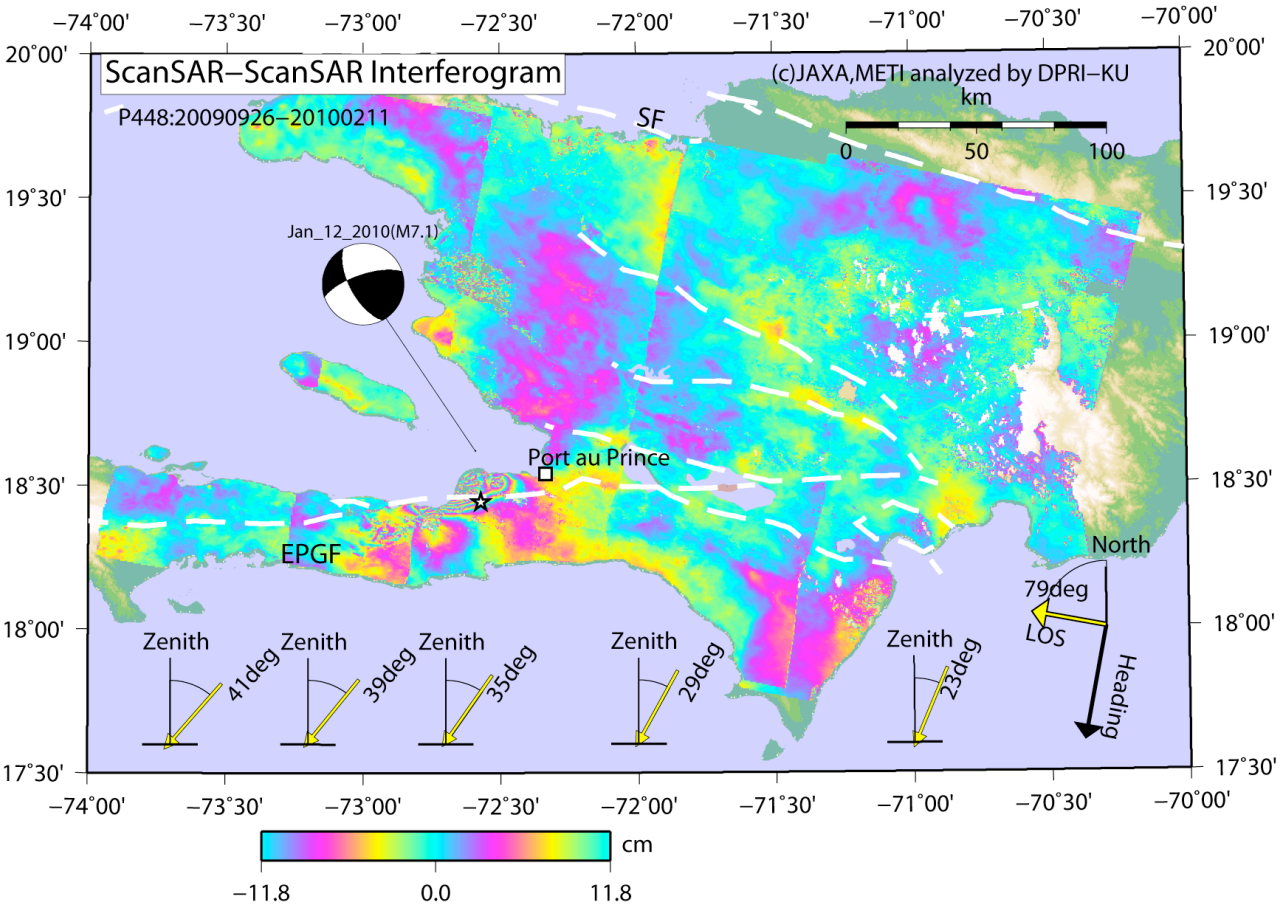

Supplementary Figure S5. Interferogram derived from ScanSAR images acquired on 26 September 2009 and 11 February 2010. The thick yellow arrow indicates the line-of-sight (LOS) direction, and the black arrow denotes the satellite heading. Thin yellow arrows indicate the incidence angle for each swath. See also the legend for Figure 2.

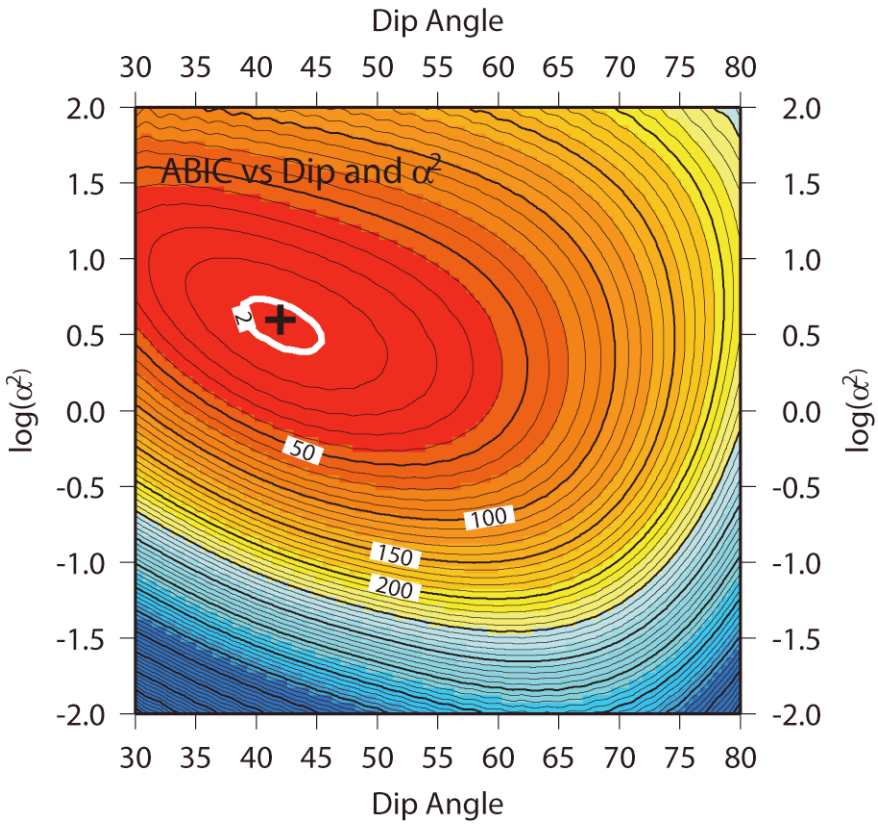

Supplementary Figure S6. Contour map of ABIC against $\log \alpha^2$ and dip angle. The cross shows the point of ABIC minimum. The interval for black contours is 20, whereas the white contour indicates the range of ABIC values larger than the minimum by increments of two.

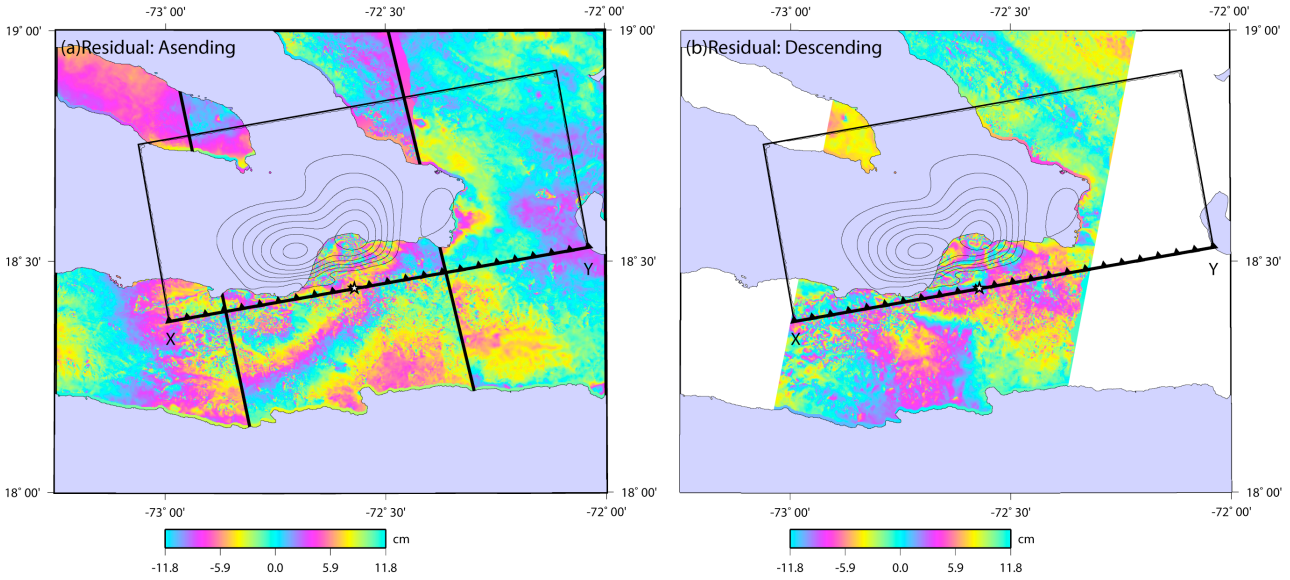

Supplementary Figure S7. Residuals for interferograms along (a) ascending and (b) descending orbits. The rectangle shows the surface projection of the modelled fault plane. Thick lines on the left indicate boundaries between paths.

Supplementary Reference

1) Jarvis, A., Reuter, H.I., Nelson, A., & Guevara, E. Hole-filled SRTM data V4. International Center for Tropical Agriculture (CIAT), http://www.srtm.csi.cgiar.org (2008).